International Journal of Modern Physics C
Vol. 19, No. 12 (2008) 1847–1861

World Scientific
www.worldscientific.com

A PARALLEL THERMAL LATTICE BOLTZMANN MODEL WITH FLUX LIMITERS FOR MICROSCALE FLOW

M. BOTTI

CASPUR, Via dei Tizii 6/b, 00185 Rome, Italy
michela.botti@caspur.it

G. GONNELLA

Dipartimento di Fisica, Università di Bari and INFN, Sezione di Bari
Via Amendola 173, 70126 Bari, Italy
gonnella@ba.infn.it

A. LAMURA

Istituto Applicazioni Calcolo, CNR
Via Amendola 122/D, 70126 Bari, Italy
a.lamura@ba.iac.cnr.it

F. MASSAIOLI

CASPUR, Via dei Tizii 6/b, 00185 Rome, Italy
federico.massaioli@caspur.it

V. SOFONEA*

Center for Fundamental and Advanced Technical Research, Romanian Academy
Bd. Mihai Viteazul 24, 300223 Timişoara, Romania
sofonea@acad-tim.tm.edu.ro

Received 19 June 2008
Accepted 20 September 2008

We propose a thermal lattice Boltzmann model to study gaseous flow in microcavities. The model relies on the use of a finite difference scheme to solve the set of evolution equations. By adopting diffuse reflection boundary conditions to deal with flows in the slip regime, we study the micro-Couette flow in order to select the best numerical scheme in terms of accuracy. The scheme based on flux limiters is then used to simulate a micro-lid-driven cavity flow by using an efficient and parallel implementation. The numerical results are in very good agreement with the available results recovered with different methods.

*Corresponding author.

Keywords: Thermal lattice Boltzmann method; numerical scheme; microfluidics.

PACS Nos.: 47.11.-j, 05.70.Ln, 51.10.+y.

1. Introduction

Fluid mechanics and transport phenomena at microscale have been attracting growing interest in the past years especially to design new micro-electromechanical devices.[1] In such systems the mean free path of the fluid molecules are of the same order as the typical size of the device. An important consequence is the appearance of a slip velocity at the boundaries, which greatly influences the mass and heat transfer in the system. A quantity which is commonly used to characterize the influence of the mean free path λ on microflows, is the Knudsen number Kn, defined as $Kn = \lambda/L$, where L is a typical dimension of the system. In the limit $Kn < 0.001$ the fluid can be treated as a continuum with no-slip boundary conditions.[2] In the slip flow regime, $0.001 < Kn < 0.1$, the continuum limit starts to break down. Despite this, the Navier–Stokes equation coupled with slip boundary conditions may still be applied to yield accurate results.[1] When $Kn > 0.1$ a kinetic-type approach, based on the direct solution of the full Boltzmann equation or on a dynamic model such as the direct simulation Monte Carlo (DSMC),[3] is required.[4] These methods are computationally expensive. Moreover, for flows at the microscale, characterized by low Mach and Reynolds numbers,[5] it is difficult with DSMC to get reliable results due to statistical fluctuations.

In recent years, the Lattice Boltzmann Method (LBM) has been applied to study different fluid systems. The method can easily handle complex geometries and is suitable for parallel implementation.[6–8] It has been also applied to address microflows.[9,10] In this paper we describe a thermal lattice Boltzmann scheme that is used to simulate microscale flows with high accuracy in the slip flow regime. We adopt a recently introduced thermal finite difference lattice Boltzmann method (FDLBM),[11] where the relationship

$$c = \frac{\delta s}{\delta t} \tag{1}$$

among the lattice speed c and the space and timesteps δs and δt does no longer hold, as in standard *collision-streaming* LBM.[6,8] Besides more freedom to choose the discrete velocity set (use of different lattice speeds is crucial in order to release the constraint of constant temperature, as done in Ref. 11), rejection of the condition (1) in FDLBM allows one to consider multicomponent fluid systems where the masses of the component particles, as well as the lattice speeds, may be no longer identical. The use of high-order numerical schemes in FDLBM helps further to improve the numerical stability and accuracy,[12] while providing a convenient alternative to interpolation-supplemented LBM.[13,14]

In Sec. 2 of the paper, the FDLBM method is described together with the choice of boundary conditions. Two possible finite difference schemes are introduced here.

In Sec. 3 an efficient and parallel implementation of the method is given. Numerical results for micro-Couette and driven cavity flows are reported in Sec. 4 to validate our method. Finally, we draw some conclusions.

2. Thermal Lattice Boltzmann Model with Flux Limiters

The finite difference lattice Boltzmann (LB) model with variable temperature, originally developed by Watari and Tsutahara,[11] involves a set of 33 nondimensionalized velocities $e_{00} = 0$, $e_{ki} = [\cos(\pi(i-1)/4), \sin(\pi(i-1)/4)]c_k$, where $k = 1, \ldots, 4$, $i = 1, \ldots, 8$, and $c_k \in \{1.0, 1.92, 2.99, 4.49\}$. The corresponding distribution functions $f_{00} = f_{00}(\mathbf{x}, t)$, $f_{ki} = f_{ki}(\mathbf{x}, t)$ are defined in the nodes $\mathbf{x}$ of a square lattice and evolve according to the nondimensionalized equation

$$\partial_t f_{ki} + \mathbf{e}_{ki} \cdot \nabla f_{ki} = -\frac{1}{\tau}[f_{ki} - f_{ki}^{\mathrm{eq}}]\,, \tag{2}$$

where τ is the relaxation time.

As usual in lattice Boltzmann models,[6] the local fluid density n, velocity $\mathbf{u}$, and temperature θ are determined from the moments of the distribution functions[11]

$$n = \sum_{ki} f_{ki}\,, \tag{3}$$

$$nu_\alpha = \sum_{ki} f_{ki} e_{ki\alpha}\,, \tag{4}$$

$$n\left(\theta + \frac{u^2}{2}\right) = \frac{1}{2}\sum_{ki} f_{ki} c_k^2\,. \tag{5}$$

The equilibrium distribution functions which appear in Eq. (2),

$$f_{ki}^{\mathrm{eq}} = f_{ki}^{\mathrm{eq}}(\mathbf{x}, t) = nF_k s_{ki} \tag{6}$$

are expressed using the series expansion $s_{ki} = s_{ki}(\theta, \mathbf{u})$ up to fourth order[11] with respect to the Cartesian components u_α ($\alpha = 1, 2$) of the fluid velocity (summation over repeated Greek indices is understood):

$$\begin{aligned} s_{ki} = {} & \left(1 - \frac{u^2}{2\theta} + \frac{u^4}{8\theta^2}\right) + \frac{1}{\theta}\left(1 - \frac{u^2}{2\theta}\right) e_{ki\xi} u_\xi + \frac{1}{2\theta^2}\left(1 - \frac{u^2}{2\theta}\right) e_{ki\xi} e_{ki\eta} u_\xi u_\eta \\ & + \frac{1}{6\theta^3} e_{ki\xi} e_{ki\eta} e_{ki\zeta} u_\xi u_\eta u_\zeta + \frac{1}{24\theta^4} e_{ki\xi} e_{ki\eta} e_{ki\zeta} e_{ki\chi} u_\xi u_\eta u_\zeta u_\chi\,. \end{aligned} \tag{7}$$

The weight factors $F_k = F_k(\theta)$ in Eq. (6) depend on the local temperature $\theta = \theta(\mathbf{x}, t)$ and the speeds c_k:

$$F_k = \frac{1}{c_k^2(c_k^2 - c_{\{k+1\}}^2)(c_k^2 - c_{\{k+2\}}^2)(c_k^2 - c_{\{k+3\}}^2)} \times \left[48\theta^4 - 6(c_{\{k+1\}}^2 + c_{\{k+2\}}^2 + c_{\{k+3\}}^2)\theta^3 + (c_{\{k+1\}}^2 c_{\{k+2\}}^2 + c_{\{k+2\}}^2 c_{\{k+3\}}^2 + c_{\{k+3\}}^2 c_{\{k+1\}}^2)\theta^2 - c_{\{k+1\}}^2 c_{\{k+2\}}^2 c_{\{k+3\}}^2 \frac{\theta}{4} \right], \tag{8}$$

$$F_0 = 1 - 8(F_1 + F_2 + F_3 + F_4)\,, \tag{9}$$

where for any $k \in \{1,2,3,4\}$ and $l \in \{1,2,3\}$,

$$\{k+l\} = \begin{cases} k+l\,, & (k+l \leq 4)\,, \\ k+l-4\,, & (k+l > 4)\,. \end{cases} \tag{10}$$

Since the nondimensionalized speeds c_k of the thermal LB model are no longer related to the lattice spacing δs and the time step δt, as in the standard (collision-streaming) LB models,[6,15] finite difference schemes need to be used to evolve the distribution functions in each lattice node.[11,16] If $f_{ki,j}^n = f_{ki}(\mathbf{x}_j, t)$ is the value of the distribution function f_{ki} at time t in the node $\mathbf{x}_j$ on the characteristic line along the direction i of the lattice, the updated value $f_{ki,j}^{n+1} = f_{ki}(\mathbf{x}_j, t+\delta t)$ of the distribution function f_{ki} at time $t+\delta t$ in the node $\mathbf{x}_j$ is computed using a conservative scheme involving two fluxes[17,12]

$$f_{ki,j}^{n+1} = f_{ki,j}^n - \frac{c_k \delta t}{A_i \delta s}[F_{ki,j+1/2}^n - F_{ki,j-1/2}^n] - \frac{\delta t}{\tau}[f_{ki}^n - f_{ki}^{\mathrm{eq},n}]\,, \tag{11}$$

where $A_i = 1$ for $i \in \{1,3,5,7\}$, $A_i = \sqrt{2}$ for $i \in \{2,4,6,8\}$. When using the first-order upwind finite difference scheme, the outgoing and incoming fluxes in node j along the direction i are set equal to the corresponding distribution functions:

$$F_{ki,j+1/2}^n = f_{ki,j}^n\,, \qquad F_{ki,j-1/2}^n = f_{ki,j-1}^n\,. \tag{12}$$

Flux limiter schemes,[17,12,18–20] which improve the first-order upwind scheme and are of second order with respect to the lattice spacing δs, may be considered in order to reduce numerical errors, by setting

$$F_{ki,j+1/2}^n = f_{ki,j}^n + \frac{1}{2}\left(1 - \frac{c_k \delta t}{A_i \delta s}\right)[f_{ki,j+1}^n - f_{ki,j}^n]\Psi(\Theta_{ki,j}^n)\,, \tag{13}$$

$$F_{ki,j-1/2}^n = F_{ki,(j-1)+1/2}^n\,. \tag{14}$$

Here $\Psi(\Theta_{ki,j}^n)$ is the flux limiter and

$$\Theta_{ki,j}^n = \frac{f_{ki,j}^n - f_{ki,j-1}^n}{f_{ki,j+1}^n - f_{ki,j}^n} \tag{15}$$

is the smoothness function. In this paper, we restrict ourselves to the Monitorized Central Difference (MCD) flux limiter scheme

$$\Psi(\Theta^n_{ki,j}) = \begin{cases} 0\,, & \Theta^n_{ki,j} \le 0\,, \\ 2\Theta^n_{ki,j}\,, & 0 \le \Theta^n_{ki,j} \le \dfrac{1}{3}\,, \\ \dfrac{(1+\Theta^n_{ki,j})}{2}\,, & \dfrac{1}{3} \le \Theta^n_{ki,j} \le 3\,, \\ 2\,, & 3 \le \Theta^n_{ki,j}\,, \end{cases} \tag{16}$$

since other limiters give similar results.[17,12,21]

Diffuse reflection boundary conditions[22–24] are considered in this paper to allow for variable Knudsen number during simulations. According to these conditions, the distribution functions whose velocities point to the wall in the normal direction mix separately from the distribution functions with velocities orientated along the diagonals of the square lattice. The black squares in Fig. 1, whose indices are $(j = 1/2, l)$ and $(j = 1/2, l + 1/2)$, $l = 0, 1, \ldots$, denote the mixing points on the wall. The wall is located half lattice spacing between the ghost nodes, and the fluid nodes and the corresponding (unknown) values of the particle number density are $n_w^{1/2,l}$ and $n_w^{1/2,l+1/2}$.

Because of the particle-wall interactions, the distribution functions of fluid particles reflected by the walls become Maxwellian.[1] Following the discretization of the velocity space in the LBM, the Maxwellian distribution function is replaced by the set of equilibrium distribution functions (6). We express the distribution functions

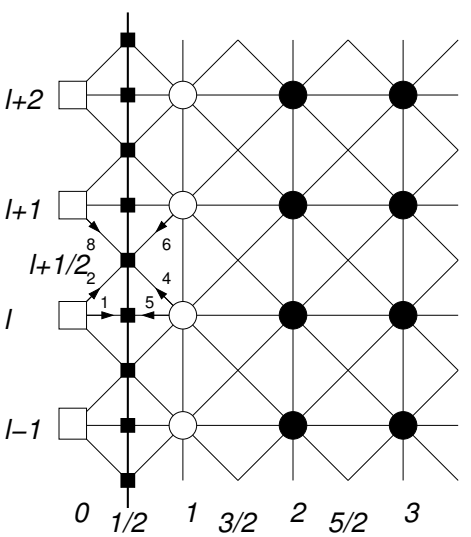

Fig. 1. Diffuse reflection boundary conditions: □ — ghost nodes, ○ — boundary nodes, • — bulk nodes, ■ — wall points where the distribution functions f_{ki} ($i = 1, 2, 8$) follow the Maxwellian distribution law.

of reflected particles in wall nodes using an interpolation procedure involving the values of the distribution functions $f_{k1}^{0,l}$, $f_{k2}^{0,l}$, and $f_{k8}^{0,l+1}$ $(l = 0, 1, \ldots)$, defined in the ghost nodes outside the wall and get $(k = 1, \ldots, 4)$:

$$\frac{f_{k1}^{0,l} + f_{k1}^{1,l}}{F_k(\theta_w) s_{k1}(\theta_w, \mathbf{u}_w)} = 2n_w^{1/2,l}\,, \tag{17}$$

$$\frac{f_{k2}^{0,l} + f_{k2}^{1,l+1}}{F_k(\theta_w) s_{k2}(\theta_w, \mathbf{u}_w)} = \frac{f_{k8}^{0,l+1} + f_{k8}^{1,l}}{F_k(\theta_w) s_{k8}(\theta_w, \mathbf{u}_w)} = 2n_w^{1/2,l+1/2}\,. \tag{18}$$

Moreover, the following equations are derived from the requirement of no mass flux perpendicular to the wall in the mixing nodes:

$$\sum_k c_k f_{k5}^{1,l} = \sum_k c_k f_{k1}^{0,l}\,, \tag{19}$$

$$\sum_k c_k [f_{k4}^{1,l} + f_{k6}^{1,l+1}] = \sum_k c_k [f_{k2}^{0,l} + f_{k8}^{0,l+1}]\,. \tag{20}$$

Equations (17)–(20) allow us to get the values of the distribution functions in the ghost nodes $(0, l)$ and $(0, l+1)$. These values are needed in Eqs. (11)–(14) to update the corresponding distribution functions in the lattice nodes located near the wall (for these nodes, the MCD scheme is reduced to the first-order upwind scheme by setting $\Psi(\Theta_{ki,j}^n) = 0$).

A characteristic of microscale fluid flow is the nonvanishing value of the Knudsen number.[1] In this paper we use the nondimensionalized density-dependent relaxation time[16] $\tau = \Lambda/\bar{n}\bar{c}$ that allows us to control the value of the Knudsen number $Kn = \tau\bar{c} = \Lambda/\bar{n}$ during LB simulations by conveniently setting the mean value $\bar{n}$ of the fluid density.[16,23,24] The nondimensionalized constant $\Lambda = 10^6$, which enters the expression of τ, is related to the diameter of the fluid particles and the characteristic length of the fluid flow domain, while $\bar{c} = \sqrt{\pi\theta/2}$ is the nondimensionalized average speed of the fluid particles in the two-dimensional system.[16,25]

3. Parallel Code Implementation

The target platform for the implementation is a cluster architecture. Most of development and all production took place on a cluster of dual processor 2.4 GHz AMD Opteron nodes, Infiniband interconnected. A cluster of 8-way 1.9 GHz IBM Power 5 nodes was used during development, to better characterize the code behavior. The Finite Difference Thermal Lattice Boltzmann Model (FDTLBM) is implemented in Fortran 90, parallelized with MPI.[26]

The two-dimensional domain is decomposed along the vertical direction, so that each process works on a chunk of horizontal lines. Each portion of the domain includes a frame of ghost nodes. At each time step, the values in the top and bottom node lines of each slice are replicated in the ghost node lines of the neighboring slices, so that the bulk of each slice can be updated as if there were no decomposition at

all. The top ghost line and the bottom ghost line of the top and bottom slices, respectively are used to implement the boundary conditions. When the latter is periodic, as in the case described in Sec. 4.1, the first and the last processes (MPI ranks 0 and $n_{\text{proc}} - 1$) are assumed to be contiguous as on a ring topology. Left and right ghost lines of each slice are used to implement lateral boundary conditions.

The code makes heavy use of Fortran 90 array-syntax, to implement the differential operators. The obvious advantage in using array syntax is that formulae are translated to code in a clear, compact form, without sacrificing readability. Array syntax is often a concern, as there are situations in which compilers produce inefficient executable code in comparison to the same computation expressed with explicit loops. This was not the case with this code, probably because of the very regular structure of the FDTLBM scheme. Our tests were performed with the IBM XL Fortran 10.1 compiler on the IBM platform, and the PGI 6.2 Fortran compiler on the AMD platform. They showed that a Fortran 77 style version of the code, where equations are computed within loop nests on the two-dimensional lattice, is as fast as the F90 version. Actually, IBM XL Fortran yielded approximately 15% better performance with the array-syntax version.

An analysis of the computational portions of the application, using hardware performance counters, shows a higher speed and a slightly higher efficiency of the code on an IBM processor (0.62 GFlops, 8.2% of peak) with respect to an AMD CPU (0.35 GFlops, 7.2% of peak). This is not surprising, as the scheme is quite demanding in terms of memory accesses, and the IBM processors benefit from ampler caches and significantly higher memory bandwidth.

Table 1 shows run times for 2500 timesteps of the simulation reported in Sec. 4.2 for $H = 2$. Timing for one AMD CPUs are not available, because the total memory needed for this case amounts to 5.5 GB, too large to fit in a single cluster node. As can be seen from the measurements, speedup is sligthly superlinear, even if the data set accessed by each process at each time step exceeds the size of the processor cache (1 MB for the AMD Opteron, 32 MB for the IBM Power 5). However, the compiler automatically generates temporary arrays to host intermediate terms of array syntax expressions. These temporary variables are heavily accessed during computations and benefit from the bigger amount of total cache resulting from using more processors. The IBM system has a slower node interconnection than the AMD cluster, but each IBM node contains eight processors, instead of only two. Thus, a suitable distribution of processes to nodes allowed for the use of shared

Table 1. Run times (s) for 2500 timesteps on a grid with 500×1000 nodes.

Number of processors	AMD Opteron cluster	IBM Power 5 cluster
1	N.A.	5059
4	1812	1178
8	868	542
16	380	230

memory for most interprocess communications. This, together with faster code execution, makes the IBM cluster run 37% faster on average than the Opteron one.

A real simulation involves more than computations, as fields must be saved at suitable intervals for further data analyses. The frequency of I/O operations depends on the dynamics of the problem, and the time needed to save data to disks can vary depending on many factors, ranging from the type of file system used to the instantaneous load of the overall computing system. To give a more practical reference for the code performance, the $H = 1$, $Kn = 0.001$ lid cavity simulation reported in Sec. 4.2, involving 6 000 000 timesteps on a 500×500 grid, ran on 16 AMD processors for a total of 171 elapsed hours. As a comparison, the $H = 2$, $Kn = 0.01$ lid cavity simulation, involving 1 700 000 timesteps on a 1000×500 grid, run on 16 AMD processors for a total of 92 elapsed hours.

4. Numerical Results

4.1. *Micro-Couette flow*

To validate the LB model in the slip flow regime, we considered the well-known Couette flow between two parallel vertical walls having the same temperature $\theta_w = 1.0$. The left and right walls move with velocities $u_{wl} = -0.1$ and $u_{wr} = 0.1$, respectively. The distance between the walls was set to $L = 1$ (nondimensionalized units), while the lattice spacing $\delta s = 1/N$ is related to the number N of nodes per unit length. For relatively small values of the Knudsen number ($Kn < 0.1$), one may use the Navier–Stokes equations to derive the following analytical solutions[1,16,27] for the transversal profiles of the vertical component $u_y(x)$ of the fluid velocity and the temperature $\theta(x)$:

$$u_y\left(x - \frac{L}{2}\right) = Ax\,, \qquad \theta\left(x - \frac{L}{2}\right) = Bx^2 + C\,, \tag{21}$$

where

$$A = \frac{u_{wr} - u_{wl}}{1 + 2Kn}\,, \qquad B = -\frac{\eta}{2\kappa}A^2\,, \qquad C = \theta_w + \frac{\eta}{8\kappa}A^2(1 + 4hKn)\,. \tag{22}$$

In the relations above, $\eta = n\theta\tau$ is the dynamic viscosity of the fluid, $\kappa = 2n\theta\tau$ is its heat conductivity, and $h = 4/3$ for the thermal LB model considered in this paper.[16]

Figure 2 shows the transversal profiles of the vertical component $u_y(x)$ of the fluid velocity, as well as of the temperature $\theta(x)$, density $n(x)$, and pressure $p(x) = n(x)\theta(x)$, recovered in the stationary state using the first-order upwind scheme with two values of N, when $\bar{n} = 10^8$ and $Kn = 0.01$. The velocity and temperature profiles in Fig. 2 are compared to the analytical solutions, Eq. (21), while density and pressure profiles are compared to $\bar{n}\bar{\theta}/\theta(x)$ and $\bar{n}\bar{\theta}$, respectively, where $\bar{\theta} = B/12 + C$ is the mean temperature. Although the velocity profiles agree very well with the analytical solution for both $N = 50$ and $N = 500$, higher temperature

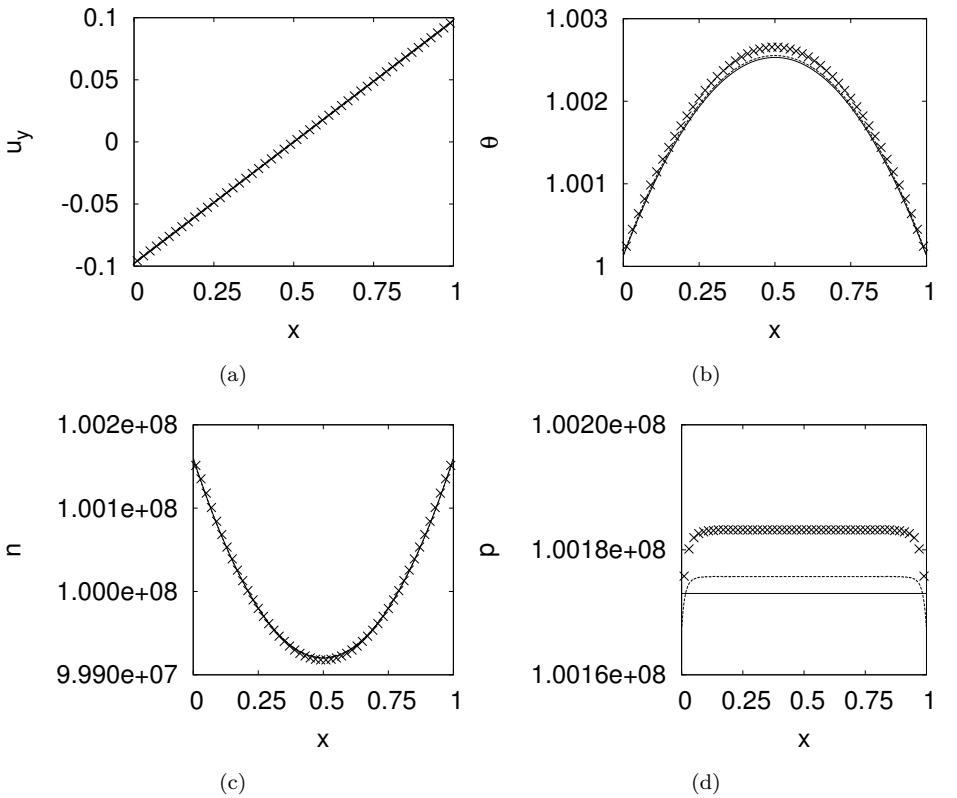

Fig. 2. Transversal profiles of fluid velocity (a), temperature (b), density (c), and pressure (d) in Couette flow, recovered using the first-order upwind scheme for $N = 50$ ($\times$) and $N = 500$ ($---$). The full line is the analytical solution.

values are noticed in the central flow domain, with respect to the corresponding analytical solution. The higher temperature values are due to the supplementary heat dissipation generated by the spurious velocity, which plagues LB simulation results in the presence of density gradients when using the first-order upwind scheme.[28] Establishment of a density gradient [Fig. 2(c)] normal to the flow direction in Couette flow is required in order to preserve constant pressure in the equilibrium state [Fig. 2(d)]. When using the MCD flux limiter scheme of second order with respect to the lattice spacing δs, the agreement between the temperature profiles and the analytical solution improves substantially for all values of N (see Fig. 3).

According to the theory developed in Ref. 28, when using the first-order upwind scheme, the spurious velocity is proportional to the fluid density gradient, as well as to the lattice spacing δs. Temperature values clearly approach the analytical solution when the lattice spacing δs becomes smaller due to larger N. This behavior is related to the corresponding reduction of the spurious velocity, i.e., the x-component of the fluid velocity established during LB simulation [Fig. 4(a)]. For a given lattice spacing δs, the spurious velocity is always much smaller when using

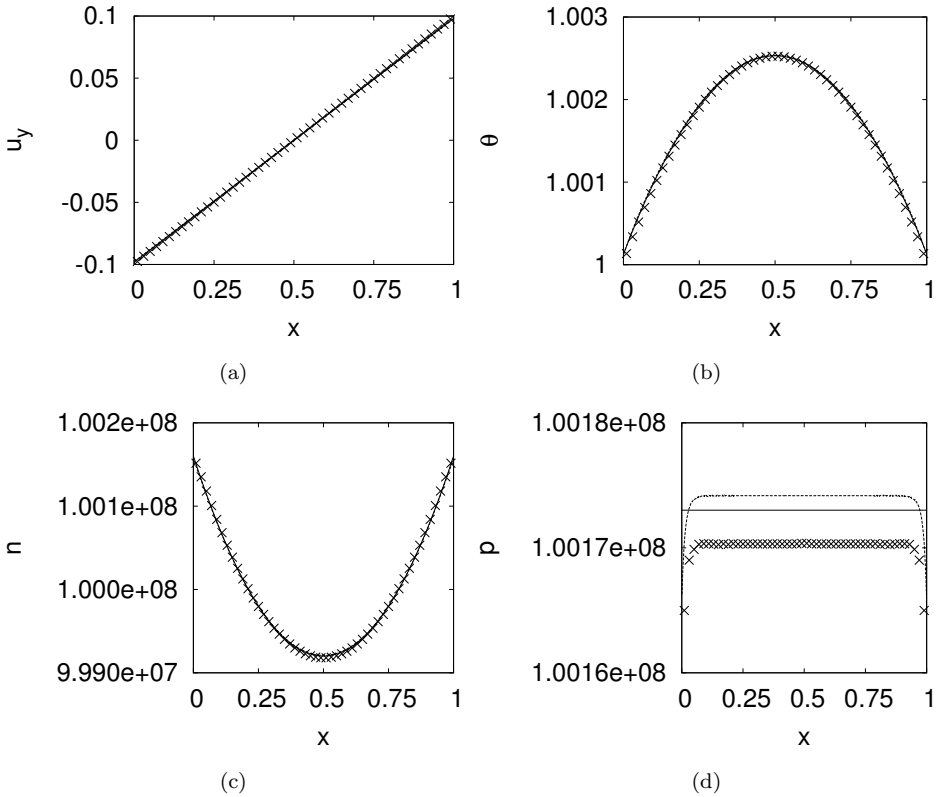

Fig. 3. Transversal profiles of fluid velocity (a), temperature (b), density (c), and pressure (d) in Couette flow, recovered using the MCD flux limiter scheme for different values of $N = 50$ ($\times$) and $N = 500$ ($- - -$). The full line is the analytical solution.

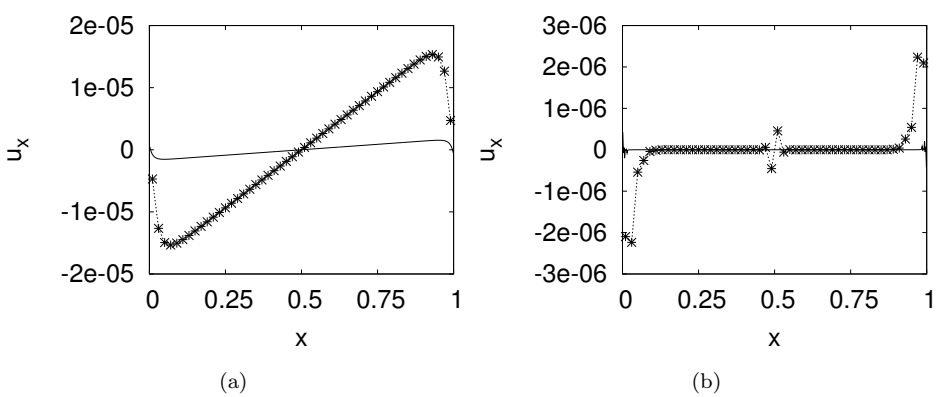

Fig. 4. Spurious velocity observed in the x-direction (same direction as the density gradient) when using the first-order upwind scheme (a) or the MCD flux limiter scheme (b) for different values of $N = 50(\star)$, $500(- - -)$.

a second-order scheme like MCD [Fig. 4(b)]. For this reason, the MCD flux limiter scheme was chosen for investigating the driven cavity flow in the following section.

4.2. *Driven cavity flow*

We considered two-dimensional driven cavities where three walls are at rest and the upper one moves rightward with velocity u_w. All the walls are kept at the same temperature $\theta_w = 1.0$. The simulated cavities have the length $L = 1$ and heights $H = 1$ or $H = 2$ (nondimensionalized units) with lattice spacing $\delta s = 1/500$. We considered the cases with average density $\bar{n} = 10^9,\ 10^8,\ 2 \times 10^7$ to simulate $Kn = 0.001, 0.01, 0.05$.[16] The value of u_w is chosen in such a way that the Reynolds number $\mathrm{Re} = nu_wL/\eta$ is fixed to be 1.0. The Mach number $\mathrm{Ma} = u_w/c_s$ is then less than 0.05, $c_s = \sqrt{2\theta}$ being the speed of sound.

Figures 5 and 6 show plots of the velocity streamlines for $H = 1$ and 2, respectively. In each figure, results are reported for various values of the Knudsen number. The flow is always symmetric with respect to $x = L/2$. In the case $L = H$, a single vortex is established. When $H = 2L$, we observe that a second vortex is formed below the upper one when increasing Kn from 0.001 to 0.01. The second vortex is still centered in the cavity. If Kn is further increased, secondary eddies are created

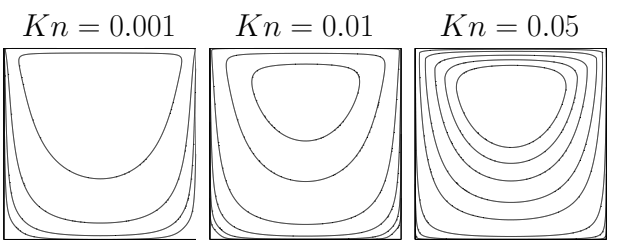

Fig. 5. Velocity streamlines for various values of Kn and $H = 1$.

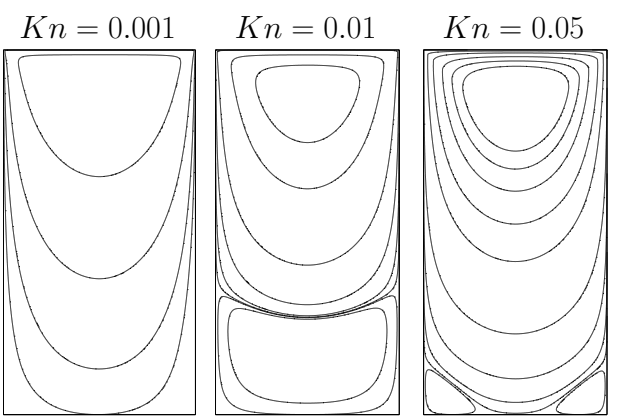

Fig. 6. Velocity streamlines for various values of Kn and $H = 2$.

at the two bottom corners. Our results are in agreement with the ones reported in Ref. 29.

In Fig. 7 we show the relative distance y/H of the center of the top vortex from the bottom of the cavity as a function of Kn for $H = 1$, 2. It is seen that the y position moves downward as the Knudsen number increases. Our results agree quite well with existing studies.

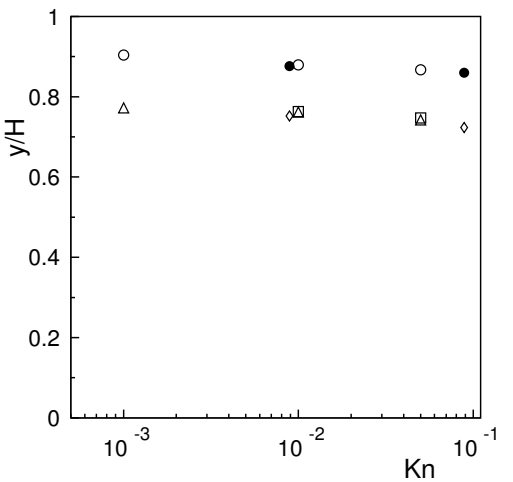

Fig. 7. Location of the center of the top vortex for various values of Kn with $H = 1$ (this study △, Naris *et al.*[29] ◇, Tang *et al.*[30] □) and $H = 2$ (this study ○, Naris *et al.*[29] ●).

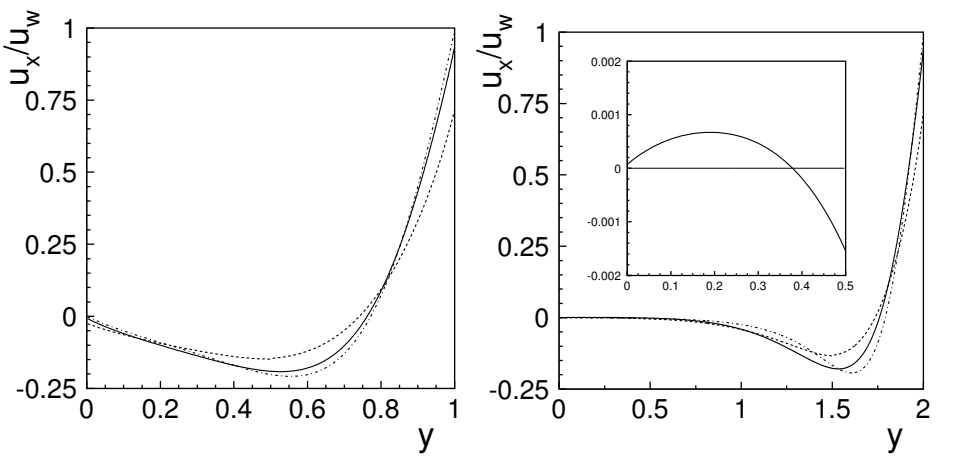

(a) (b)

Fig. 8. Profiles of the horizontal component of the velocity on a vertical line crossing the center of the cavity, for $H = 1$(a), 2(b) and different values of $Kn = 0.001$ (dotted-dashed line), 0.01 (full line), 0.05 (dashed line). The inset shows an enlargement of the profile close to the bottom of the cavity in the case with $Kn = 0.01$.

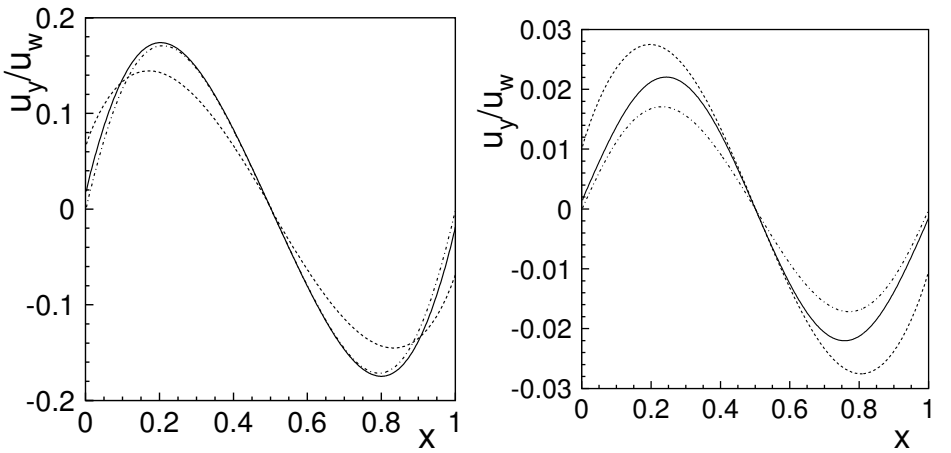

(a) (b)

Fig. 9. Profiles of the vertical component of the velocity on a horizontal line crossing the center of the cavity, for $H = 1$(a), 2 (b) and different values of $Kn = 0.001$ (dotted-dashed line), 0.01 (full line), 0.05 (dashed line).

To have more quantitative results we plotted the velocity profiles through the cavity center $(L/2, H/2)$. In Fig. 8 the horizontal component u_x is shown in the cases $H = 1$, 2 for different values of Kn along the y-axis. In the case $H = 1$ it is clearly visible that with increasing Kn, the slip velocity at the top and bottom walls increases. When $H = 2$ the slip velocity is still present at the top wall. At the lower wall the horizontal velocities are smaller compared to the previous case. In all cases, when there is a single vortex in the cavity, the velocity profiles cross the line $u_x = 0$ only once. Moreover, since there is a second vortex for $Kn = 0.01$ centered at $x = L/2$ (see Fig. 6), we enlarged the profile of the velocity u_x along the y-axis in the range [0, 0.5]. The y-position where the velocity profile crosses the line $u_x = 0$ is the center of the counter-rotating vortex.

In Fig. 9 the horizontal component u_y is shown in the cases $H = 1$, 2 for different values of Kn along the x-axis. In all cases, the slip velocity at the lateral walls increases with Kn. When $H = 2$ the slip velocity is one order of magnitude smaller than in the case $H = 1$.

Nonhomogeneous pressure and temperature fields are observed in the cavity. Typical temperature plots for $Kn = 0.05$ and $H = 1$, 2 are shown in Fig. 10. These plots are antisymmetric with respect to $x = L/2$. As Kn is decreased and we move to the continuum regime, the peaks in Fig. 10 are reduced.

5. Conclusions

In this paper a thermal lattice Boltzmann model has been proposed for microflows. It is based on the use of a second-order finite difference scheme, which enables to reach a higher numerical accuracy. The method is implemented in a parallel

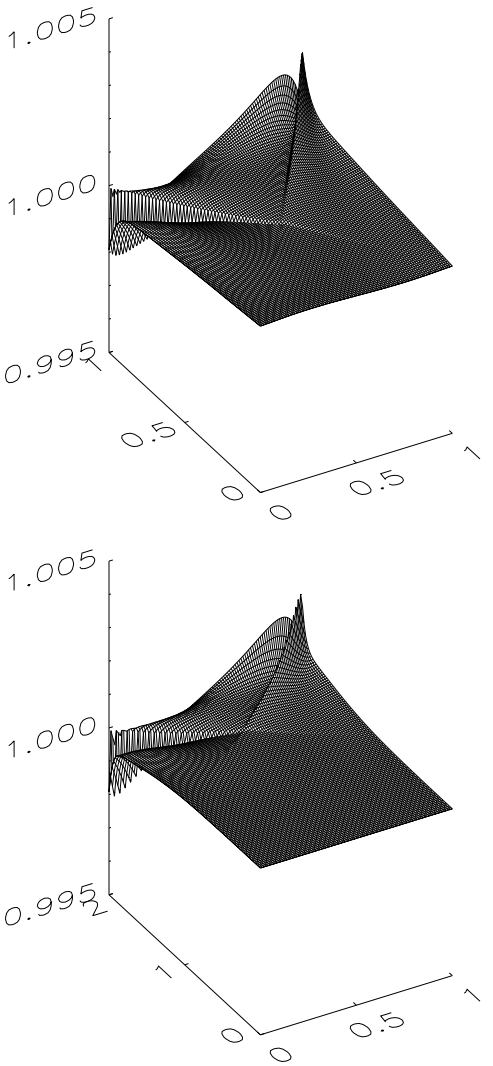

Fig. 10. Temperature plots for $H = 1$ (upper panel), 2 (lower panel) in the case with $Kn = 0.05$.

Fortran 90 code and validated with two benchmark cases. The results are in very good agreement with the available analytical and numerical studies. The present method is also able to capture thermal effects thus providing feasibility of simulating fluids with nonuniform temperature. We aim to address this task in future work.

Acknowledgments

We acknowledge CASPUR for the grant CASPUR-2005. V.S. acknowledges also the projects CEEX 11/2005 and GAR 301/2007.

References

1. G. E. Karniadakis, A. Beskok and N. Aluru, *Microflows and Nanoflows: Fundamentals and Simulation* (Springer, Berlin, 2005).
2. S. A. Schaaf and P. L. Chambre, *Flow of Rarefied Gases* (Princeton University Press, Princeton, 1961).
3. G. A. Bird, *Molecular Gas Dynamics and the Direct Simulation of Gas Flows* (Oxford University Press, Oxford, 1994).
4. C. Cercignani, *The Boltzmann Equation and its Application* (Springer, New York, 1988).
5. T. M. Squires and S. R. Quake, *Rev. Mod. Phys.* **77**, 977 (2005).
6. S. Succi, *The Lattice Boltzmann Equation for Fluid Dynamics and Beyond* (Clarendon Press, Oxford, 2001).
7. R. Benzi, S. Succi and M. Vergassola, *Phys. Rep.* **222**, 145 (1992).
8. S. Chen and G. D. Doolen, *Ann. Rev. Fluid Mech.* **30**, 329 (1998).
9. X. Nie, G. D. Doolen and S. Chen, *J. Stat. Phys.* **107**, 279 (2002).
10. F. Toschi and S. Succi, *Europhys. Lett.* **69**, 549 (2005).
11. M. Watari and M. Tsutahara, *Phys. Rev. E* **67**, 036306 (2003).
12. V. Sofonea, A. Lamura, G. Gonnella and A. Cristea, *Phys. Rev. E* **70**, 046702 (2004).
13. X. He, L. Luo and M. Dembo, *J. Comput. Phys.* **129**, 357 (1996).
14. X. He, *Int. J. Mod. Phys. C* **8**, 737 (1997).
15. D. A. Wolf–Gladrow, *Lattice Gas Cellular Automata and Lattice Boltzmann Models* (Springer, Berlin, 2000).
16. V. Sofonea and R. F. Sekerka, *Phys. Rev. E* **71**, 066709 (2005).
17. A. Cristea and V. Sofonea, *Central Eur. J. Phys.* **2**, 382 (2004).
18. G. Gonnella, A. Lamura and V. Sofonea, *Phys. Rev. E* **76**, 036703 (2007).
19. R. J. LeVeque, *Numerical Methods for Conservation Laws* (Birkhäuser, Basel, 1992).
20. E. F. Toro, *Riemann Solvers and Numerical Methods for Fluid Dynamics* (Springer, Berlin, 1999).
21. V. Sofonea and R. F. Sekerka, *Int. J. Mod. Phys. C* **16**, 1075 (2005).
22. S. Ansumali and I. V. Karlin, *Phys. Rev. E* **66**, 026311 (2002).
23. V. Sofonea, *Phys. Rev. E* **74**, 056705 (2006).
24. V. Sofonea, *Europhys. Lett.* **76**, 829 (2006).
25. W. G. Vincenti and C. H. Kruger, *Introduction to Physical Gas Dynamics* (John Wiley and Sons, New York, 1965).
26. www-unix.mcs.anl.gov/mpi/
27. A. D'Orazio and S. Succi, *Future Gen. Comput. Sys.* **20**, 935 (2004).
28. A. Cristea and V. Sofonea, *Int. J. Mod. Phys. C* **14**, 1251 (2003).
29. S. Naris and D. Valougeorgis, *Phys. Fluids* **17**, 097106 (2005).
30. G. H. Tang, W. Q. Tao and Y. L. He, *Phys. Fluids* **17**, 058101 (2005); *Int. J. Mod. Phys. C* **18**, 805 (2007).